



HAL
open science

Passivation-Induced Cr and Mo Enrichments of 316L Stainless Steel Surfaces and Effects of Controlled Pre-Oxidation

Benjamin Lynch, Zuocheng Wang, Li Ma, Eirini-Maria Paschalidou, Frédéric
Wiame, Vincent Maurice, Philippe Marcus

► **To cite this version:**

Benjamin Lynch, Zuocheng Wang, Li Ma, Eirini-Maria Paschalidou, Frédéric Wiame, et al..
Passivation-Induced Cr and Mo Enrichments of 316L Stainless Steel Surfaces and Effects of Controlled
Pre-Oxidation. *Journal of The Electrochemical Society*, 2020, 167 (14), pp.141509. hal-03032861

HAL Id: hal-03032861

<https://hal.science/hal-03032861>

Submitted on 1 Dec 2020

HAL is a multi-disciplinary open access archive for the deposit and dissemination of scientific research documents, whether they are published or not. The documents may come from teaching and research institutions in France or abroad, or from public or private research centers.

L'archive ouverte pluridisciplinaire **HAL**, est destinée au dépôt et à la diffusion de documents scientifiques de niveau recherche, publiés ou non, émanant des établissements d'enseignement et de recherche français ou étrangers, des laboratoires publics ou privés.

OPEN ACCESS

Passivation-Induced Cr and Mo Enrichments of 316L Stainless Steel Surfaces and Effects of Controlled Pre-Oxidation

To cite this article: Benjamin Lynch *et al* 2020 *J. Electrochem. Soc.* **167** 141509

View the [article online](#) for updates and enhancements.

239th ECS Meeting

with the 18th International Meeting on Chemical Sensors (IMCS)

ABSTRACT DEADLINE: DECEMBER 4, 2020



May 30-June 3, 2021

SUBMIT NOW →



Passivation-Induced Cr and Mo Enrichments of 316L Stainless Steel Surfaces and Effects of Controlled Pre-Oxidation

Benjamin Lynch,^{1b} Zuocheng Wang,^{1b} Li Ma,^a Eirini-Maria Paschalidou,^b Frédéric Wiame,^{1b} Vincent Maurice,^z and Philippe Marcus^{*,z}

PSL Research University, CNRS - Chimie ParisTech, Institut de Recherche de Chimie Paris (IRCP), Physical Chemistry of Surfaces Group, 75005 Paris, France

Passivation mechanisms and the effects of controlled pre-oxidation, by exposure to oxygen at ultra-low pressure, on Cr and Mo surface enrichments were investigated on polycrystalline AISI 316L stainless steel surfaces with direct transfer between surface preparation and analysis by X-ray photoelectron spectroscopy and electrochemistry. Exposure to sulfuric acid at open circuit potential causes preferential dissolution of oxidized iron species, which promotes Cr³⁺ and Mo^{4+/6+} enrichments. Anodic passivation forces oxide film re-growth and Cr³⁺ dehydroxylation with no loss of Mo^{4+/6+} pre-enrichment. Ultra-low pressure pre-oxidation promotes Mo^{4+/6+} enrichment in the exchange outer hydroxide layer of the passive film, with no Mo⁰ depletion in the modified alloy region underneath the oxide film at open circuit potential, and under anodic passivation. Mo^{4+/6+} enrichment improves protectiveness against transient active dissolution during the active/passive transition.

© 2020 The Author(s). Published on behalf of The Electrochemical Society by IOP Publishing Limited. This is an open access article distributed under the terms of the Creative Commons Attribution 4.0 License (CC BY, <http://creativecommons.org/licenses/by/4.0/>), which permits unrestricted reuse of the work in any medium, provided the original work is properly cited. [DOI: 10.1149/1945-7111/abc727]



Manuscript submitted September 25, 2020; revised manuscript received October 29, 2020. Published November 11, 2020. *This paper is part of the JES Focus Issue on Characterization of Corrosion Processes in Honor of Philippe Marcus.*

Passivity is a key property for the durable use of metals and alloys, since it provides nanometer-thick, long-term self-protection against corrosion, thanks to the formation at the surface of a self-healing oxide film, the passive film. On ferritic and austenitic stainless steels (SS), efficient passivity relies on a marked Cr³⁺ enrichment of the passive film resulting from the higher stability in corrosive environments of Cr³⁺ compared to Fe^{2+/3+} oxide/hydroxide species.^{1–8} Only very little Ni²⁺ is present when detected in the passive films formed on austenitic SS, and the metallic alloy region underneath the oxide is enriched in Ni⁰.^{9–16} Molybdenum is added in stainless steels, e.g., in austenitic AISI 316L, in order to increase corrosion resistance in chloride-containing environments. The passive film breakdown can lead to the initiation of localized corrosion by pitting with costly consequences, as well as potentially putting the environment and people's health at risk. On Mo-containing SS, the passive films are also ultrathin, but their composition includes Mo⁴⁺ and Mo⁶⁺ oxide species at a few at% level.^{11,14,16–25} There is still a debate on the origin of the beneficial role of molybdenum: does molybdenum mitigate passive film breakdown^{9,11,17,19–21,26–33} or promote passive film repair?^{11,13,18,24,29,31–34}

Recent studies have shown that chemical/structural heterogeneities/defects, depleted in Cr³⁺, can be produced at the nanometric scale, with the pre-passivation mechanism governing the initial growth of the surface oxide film.^{35–37} Nanoscale compositional heterogeneities were also inferred from studies of mature passive films^{16,38} and can be considered as weak points at the origin of the subsequent loss of stability.^{7,8} Improving the stability of the corrosion protection requires developing strategies to reinforce and/or avoid these weak points. As well as this, it is vital to further understand the alterations brought about by exposure to aqueous environments and electrochemical passivation of oxide pre-covered SS surfaces. Recently, this was addressed on native oxide-covered polycrystalline AISI 316L surfaces.^{39–41} The previously reported^{11,12,14,16,19–21,23} bilayer structure of the passive film was confirmed. However, it was found to already develop in the native

oxide film, formed after surface polishing. Cr³⁺ was found more concentrated in the inner layer and Fe³⁺ in the outer layer, together with Mo^{4+/6+}.^{39,40} Electrochemical passivation in a chloride-free sulfuric acid solution did not alter the bilayer structure of the surface oxide but promoted the Cr and Mo enrichments, owing to the surface stability and preferential dissolution of Fe^{2+/3+} in acid solution as previously proposed.^{42–45} Thanks to a transfer line avoiding exposure to ambient air between electrochemical treatment and surface analysis, it was shown that Cr³⁺ and Mo^{4+/6+} enrichment occurred already at open circuit potential prior to anodic polarization.⁴⁰ Anodic pre-passivation in Cl-free solution was also found to block the entry of chloride in the passive film observed in a Cl-containing solution.⁴¹

In the present work, we address the effect of controlled pre-oxidation of a 316L SS surface on the compositional modifications brought by passivation in aqueous acid solution. Experiments were carried out in an ultra-high-vacuum (UHV) system with an attached glovebox where electrochemical alterations could be carried out. The UHV system allowed for the testing of different well-controlled pre-oxidation scenarios starting from an initial oxide-free surface, as previously studied on FeCrNi.⁴⁶ The attached Ar-filled glovebox allowed for the electrochemical alterations to be carried out without modifications brought about by transfer to air. The results bring new insight into how well-controlled pre-oxidation can promote Mo enrichment and improve protectiveness before anodic passivation.

Experimental

A closed system, with direct sample transfer, which ensures that there is no exposure to ambient air, between a UHV platform, for surface preparation and analysis, and a glove box equipped for electrochemistry was used.⁴⁶ Surface cleaning, pre-oxidation, and XPS analysis were performed in the UHV platform with a base pressure lower than 10^{−10} mbar. Electrochemical experiments were performed in the directly connected and Ar-filled glove box (Ar gas purity 99.998%, overpressure with respect to atmospheric pressure ΔP = 215 Pa). In presence of the aqueous solutions needed for electrochemistry, the residual concentrations of O₂ and H₂O in the glove box were typically around 350 and 150 ppm, respectively, corresponding to a relative humidity of 0.7%–0.5% at 20 °C–25 °C.

Disk-shaped samples of polycrystalline AISI 316L austenitic SS, with bulk composition of Fe–19Cr–13Ni–2.7Mo wt% (Fe–20Cr–12Ni–1.6Mo at%) were used. As in previous studies,^{39–41} the surface was first prepared by mechanical grinding

*Electrochemical Society Fellow.

^aPresent addresses: Department of Materials Science, Fudan University, Shanghai, 200433, China; Zhuhai Fudan Innovation Institute, Hengqin New Area, Zhuhai, 519000, China.

^bPresent address: Department of Chemistry-Ångström, Uppsala University, Uppsala, SE-751 21, Sweden.

^zE-mail: vincent.maurice@chimieparistech.psl.eu; philippe.marcus@chimieparistech.psl.eu

with emery paper of successive 1200 and 2400 grades and then polishing with diamond suspensions of successive 6, 3, 1, and 0.25 μm grades. Cleaning and rinsing were performed after each polishing step in successive ultrasonicated baths of acetone, ethanol, and Millipore[®] water (resistivity > 18 $\text{M}\Omega\cdot\text{cm}$). Filtered compressed air was used for drying. The sample is covered by the native oxide, which is formed as soon as polishing is stopped. The native oxide-covered surface state studied in the present work was kept for a short time (10 min) in ambient air before the transfer under UHV for surface characterization or to the Ar-filled glove box for electrochemical treatment.

In the UHV system, the surface can be further cleaned by repeated Ar^+ ion sputtering (3 kV, 50 μA , 10 min) in order to remove the surface oxide, as verified by XPS. The growth of the surface oxide film can then be monitored in the UHV system by well-controlled exposure to gaseous oxygen introduced at ultra-low pressure (ULP) via a controlled leak valve. Initial oxidation performed on FeCrNi surfaces in these conditions showed that the surface is saturated at room temperature (RT) after an oxygen exposure of about 10 L ($1 \text{ L} = 1.33 \times 10^{-6} \text{ mbar}\cdot\text{s}$).³⁵ Here, it was chosen to expose the initial oxide-free surface to gaseous oxygen up to 100 L at RT, thus producing the ULP pre-oxidized surface state studied in this work.

For electrochemical treatments, the native oxide-covered surface and the surfaces prepared under UHV were transferred to the electrochemical cell under the Ar environment of the glove box. For the ULP pre-oxidized surface, transit in the glove box lasted for about 30 min corresponding to about 5×10^8 and 2×10^8 L exposures to the residuals of oxygen gas and water vapor, respectively. A micro electrochemical cell well adapted for STM measurements under electrochemical control was used.⁴⁷ The cell, made of Kel-F, contains $\sim 350 \mu\text{l}$ of electrolyte. A working electrode area of 0.16 cm^2 was used, delimited by a Viton O-ring, allowing for centering on the sample surface. The sample can thus remain attached to the sample holder needed for transfer to and from UHV. Two Pt wires served as a pseudo reference electrode (calibrated as $U (\text{V vs SHE}) = U (\text{V vs Pt}) + 0.75 \text{ V}$) and a counter electrode. The micro electrochemical cell cleaning process has been detailed elsewhere.⁴⁷ The cell was controlled by a PicoStat potentiostat and Picoscan software (Agilent Technologies).

An aqueous solution of 0.05 M H_2SO_4 , prepared from ultrapure chemicals (VWR[®]) and Millipore[®] water (resistivity > 18 $\text{M}\Omega\cdot\text{cm}$), was used as an electrolyte. Deaeration by Ar bubbling was performed for 30 min before introduction to the glove box. Polarization curves were obtained by linear scan voltammetry performed in the range of (-1.25 V , $+1.2 \text{ V}$) at a scan rate of $5 \text{ mV}\cdot\text{s}^{-1}$ after resting at open circuit potential (OCP) for 30 min. Passivation treatments were conducted at OCP (i.e. at free potential) for 30 min and with anodic polarization applied by stepping the potential to U_{pass} for 30 min after resting at OCP for 30 min. U_{pass} was selected in the potential range of minimum passive current. No cathodic pre-treatment was performed in order to avoid any reduction-induced alteration of the surface oxide films prior to passivation. All experiments were performed at room temperature.

The chemical composition of the oxidized and passivated surfaces, as well as the thickness of the surface oxides, were determined by XPS analysis. An Argus spectrometer was used with the monochromatic XM1000 MkII Al K_{α} radiation source (1486.6 eV), both from Scienta Omicron. High-resolution spectra of Fe 2p, Cr 2p, Ni 2p, Mo 3d, O 1s, S 2p, and C 1s core levels were recorded at a pass energy of 20 eV and with a step size of 0.1 eV. The take-off angle of the photoelectrons was 45° . Data processing (curve fitting) was performed with CasaXPS,⁴⁸ using an adjustable Shirley type background. Binding Energies (BE) were calibrated with respect to the Fermi level energy. The spectral decomposition method adopted for FeCrNi surfaces was applied.^{35,46} Several constraints were applied to the peak components when fitting the high-resolution spectra (BE, Full Width at Half Maximum (FWHM), line shape asymmetry) in order to achieve a more accurate and consistent fit. Intensities of the $2p_{3/2}$ – $2p_{1/2}$ spin-orbit doublets for Fe, Cr and S, as well as $3d_{5/2}$ – $3d_{3/2}$ for Mo were fixed according to their theoretical ratios. For nickel, only the Ni $2p_{3/2}$ was treated due to no overlap with the Ni $2p_{1/2}$ peak. Metallic components were fitted with an asymmetric Lorentzian curve convoluted by a Gaussian curve, denoted LA (α , β , n) where α and β correspond to variables associated with the asymmetric Lorentzian curve and n takes an integer value (0–500) relating to the degree of Gaussian form used in the convolution. For non-metallic peaks, which generally have a symmetric shape, a Lorentzian/Gaussian product formula, denoted GL(n), where n refers to the percentage of Lorentzian character, was used in most cases.

Results and Discussion

Pre-treatment effects on electrochemical passivation.—Figure 1 compares the potentiodynamic polarization curves obtained in 0.05 M $\text{H}_2\text{SO}_4(\text{aq})$ for the native oxide-covered (Nat) and the ULP pre-oxidized surfaces. The two samples have the same corrosion potential of $E_{\text{corr}} = -1.01 \pm 0.01 \text{ V/Pt}$, as expected for saturated surfaces fully covered by oxide growth. The cathodic branches do not show any marked differences suggesting similar proton reduction properties in the deaerated acid electrolyte.

In the anodic branch, the current density of the ULP pre-oxidized sample is lower prior to passivation and at the passivation potential. There is no activation peak for the ULP sample, which is in contrast with the native oxide-covered sample. The oxide film formed under ULP oxygen, and exposed to the acid solution at OCP, appears thus fully protective against active dissolution, whereas the oxide film formed after polishing and exposed to the acid solution in the same conditions appears partially protective. Comparing the densities of the anodic charge transferred in the potential range of the activation peak, between U_{corr} and $U_{\text{corr}} + 0.2 \text{ V}$, one obtains values of $1.17 \text{ mC}\cdot\text{cm}^{-2}$ for the ULP sample vs $1.55 \text{ mC}\cdot\text{cm}^{-2}$ for the Nat sample. If the charge is associated with metal consumption by dissolution ($\text{Me} \rightarrow \text{Me}^{2+} + 2 \text{e}^-$), one can estimate the equivalent thickness of metal additionally consumed from the charge excess observed for the Nat sample by taking into account the atomic density ($1.83 \times 10^{15} \text{ at}\cdot\text{cm}^{-2}$) and thickness (0.207 nm) of the (111) plane of the *fcc* structure of the alloy. From the charge excess of $0.38 \text{ mC}\cdot\text{cm}^{-2}$, one

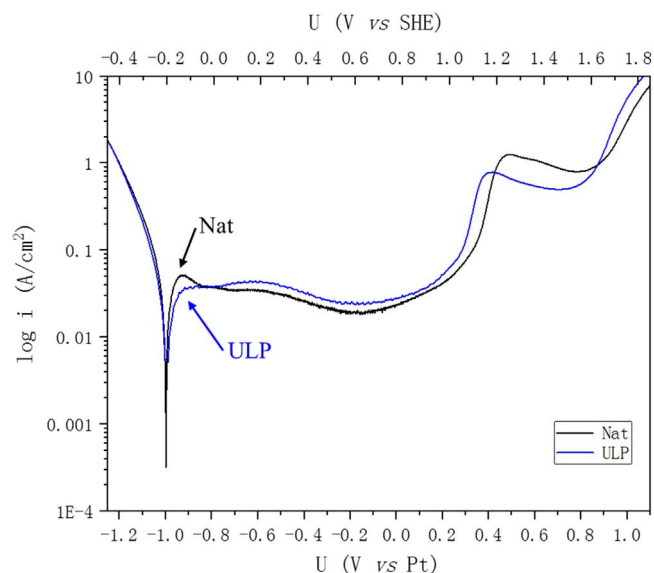


Figure 1. Potentiodynamic polarization curves for 316L surfaces prepared oxide-free in UHV environment and subsequently pre-oxidized to saturation by exposure to oxygen gas at ultra-low pressure (ULP) and for native oxide-covered surfaces formed after polishing (Nat). Recorded in 0.05 M H_2SO_4 at room temperature after 30 min rest at OCP with $5 \text{ mV}\cdot\text{s}^{-1}$ scanning rate.

finds a value of 0.14 nm of additionally consumed alloy. This low value is of the order of a fraction of a monolayer (0.66 ML). Therefore, both samples are pre-passivated by the presence of the pre-formed surface oxide films. However, the ULP pre-oxidation treatment promotes the protectiveness of the pre-passivation state since it more efficiently blocks the residual transient active dissolution observed with the native oxide-covered initial surface state.

In the passive domain, a slightly higher current density is observed for the ULP pre-oxidized sample in Fig. 1, however, the difference is within the reproducibility range of the samples and cannot be considered as significant. Similarly, no reproducible difference could be observed for the entry in the transpassive domain. In the transpassive domain, the passive film was reproducibly observed to be more protective for the ULP pre-oxidized sample than for the native oxide-covered sample, possibly owing to increased Mo enrichment.²⁵

Nature of surface species.—The XPS Fe 2p, Cr 2p and Mo 3d core-level spectra obtained for the native oxide-covered surface before and after electrochemical treatment at OCP and anodic passivation (AP) in the 0.05 M H₂SO₄(aq) electrolyte are shown in Fig. 2. Those obtained for the ULP pre-oxidized surface are shown in Fig. 3. The BE values and FWHM values of the component peaks obtained by curve fitting are compiled in Table I. These parameters were determined by a self-consistent procedure and then fixed for all the spectra analyzed in this work. Only the intensities of the peaks, compiled in Table II, were adjusted for optimizing the reconstruction.

The Cr 2p spectra show the presence of Cr⁰ and Cr³⁺ chemical states. Values of the BE splitting for the 3/2–1/2 spin-orbit doublet were 9.3, 9.7, 9.7, 8.9 and 9.3 eV for Cr⁰ (metal), Cr³⁺ (oxide) and

Cr³⁺ (hydroxide), Cr³⁺ (oxide satellite), Cr³⁺ (hydroxide satellite), respectively, similar to splitting energies reported in the literature for these species.^{35,49} The Cr³⁺ oxide component is nearly identical to that obtained in our previous work.^{35,46} The additional component assigned to Cr³⁺ hydroxide is pronounced after treatment in the H₂SO₄(aq) solution. This additional component is shifted by +1.0 eV compared to the Cr³⁺ oxide component, in good agreement with the chemical shift reported in the literature for Cr³⁺ hydroxides.^{14–16,39–41,46,50–52} No Cr⁶⁺ peak expected at a BE of ~579.5 eV⁵³ was needed to optimize the fit.

The Fe 2p spectra show the presence of the Fe⁰, Fe²⁺ and Fe³⁺ chemical states. The main oxidized iron state is Fe³⁺. Fe²⁺ is only observed at a few percent (Table II). BE splitting was 13.0, 13.5, 13.3, 13.0, 13.3 and 13.5 eV for Fe⁰ (metal), Fe²⁺ (oxide), Fe³⁺ (oxide), Fe³⁺ (hydroxide), Fe²⁺ (oxide satellite) and Fe³⁺ (oxide satellite), respectively. Similar values have been reported in the literature.^{35,54} The additional chemical states assigned to Fe³⁺ hydroxide surface species were only observed on the as-prepared native oxide-covered surface. For nickel, no Ni²⁺ oxidized state was observed after ULP pre-oxidation under UHV. It only appears in minute amounts in the form of oxide species on the as-prepared native oxide-covered surface and after anodic passivation (Table II).

The Mo 3d spectra were fitted with four 5/2–3/2 spin-orbit doublets assigned to Mo⁰ (metal) in the substrate and Mo⁴⁺ and Mo⁶⁺ cations in the surface oxide film.^{12–15,21,39–41,53,55} Spin-orbit splitting between Mo 3d_{5/2} and Mo 3d_{3/2} was found to be 3.2, 3.4, 3.3 and 3.3 eV for Mo⁰ (metal), Mo⁴⁺ (oxide), Mo⁴⁺ (hydroxide), and Mo⁶⁺ (oxide), respectively, also in line with literature values.^{39,56} The additional Mo⁴⁺ component, assigned to hydroxide (or oxyhydroxide) species,¹⁴ was needed after treatment in the H₂SO₄(aq) solution, like the Cr³⁺ hydroxide peak. A S 2s peak was

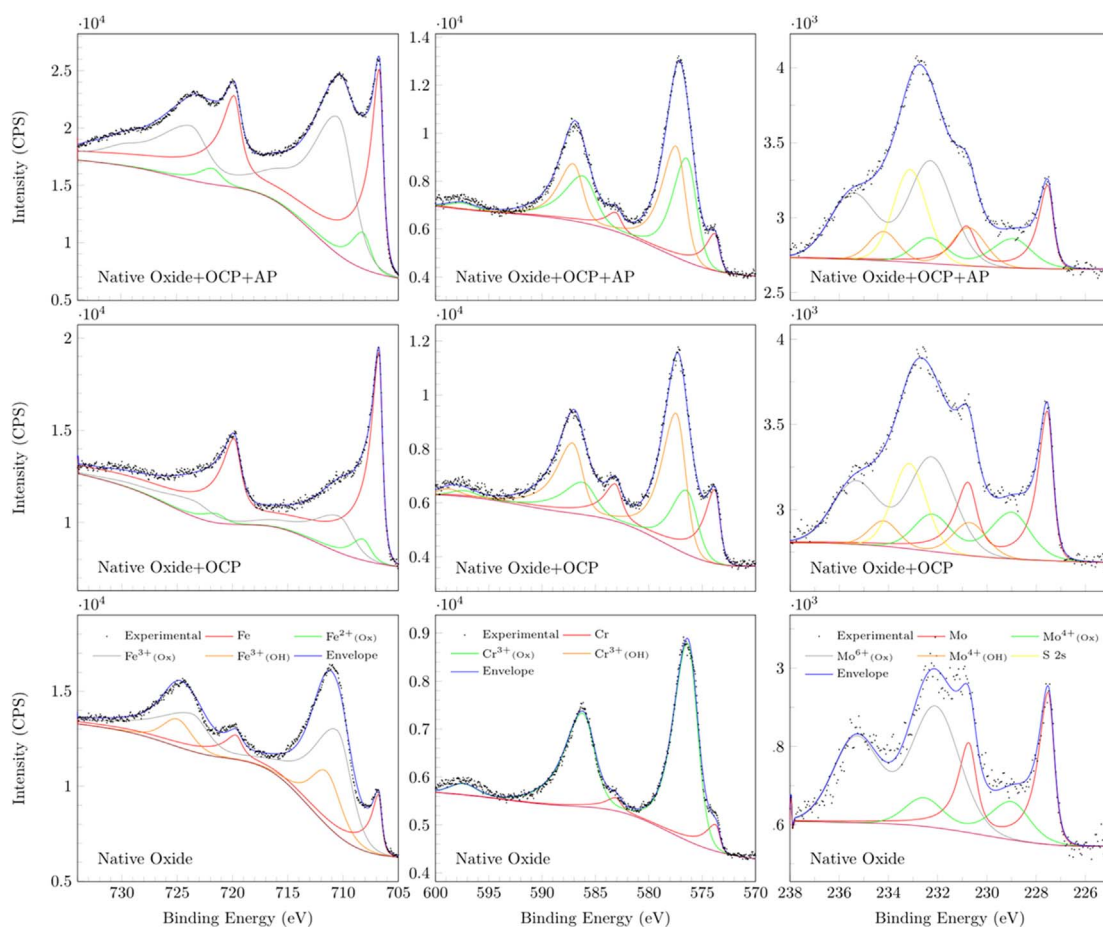


Figure 2. XPS Fe 2p, Cr 2p, Mo 3d core level spectra and their peak fitting for the native oxide-covered 316L surface (Nat) sequentially treated at open circuit potential (OCP) and under anodic polarization (AP) at $U_{\text{pass}} = -0.17$ V/Pt in 0.05 M H₂SO₄. The emission angle is 45°.

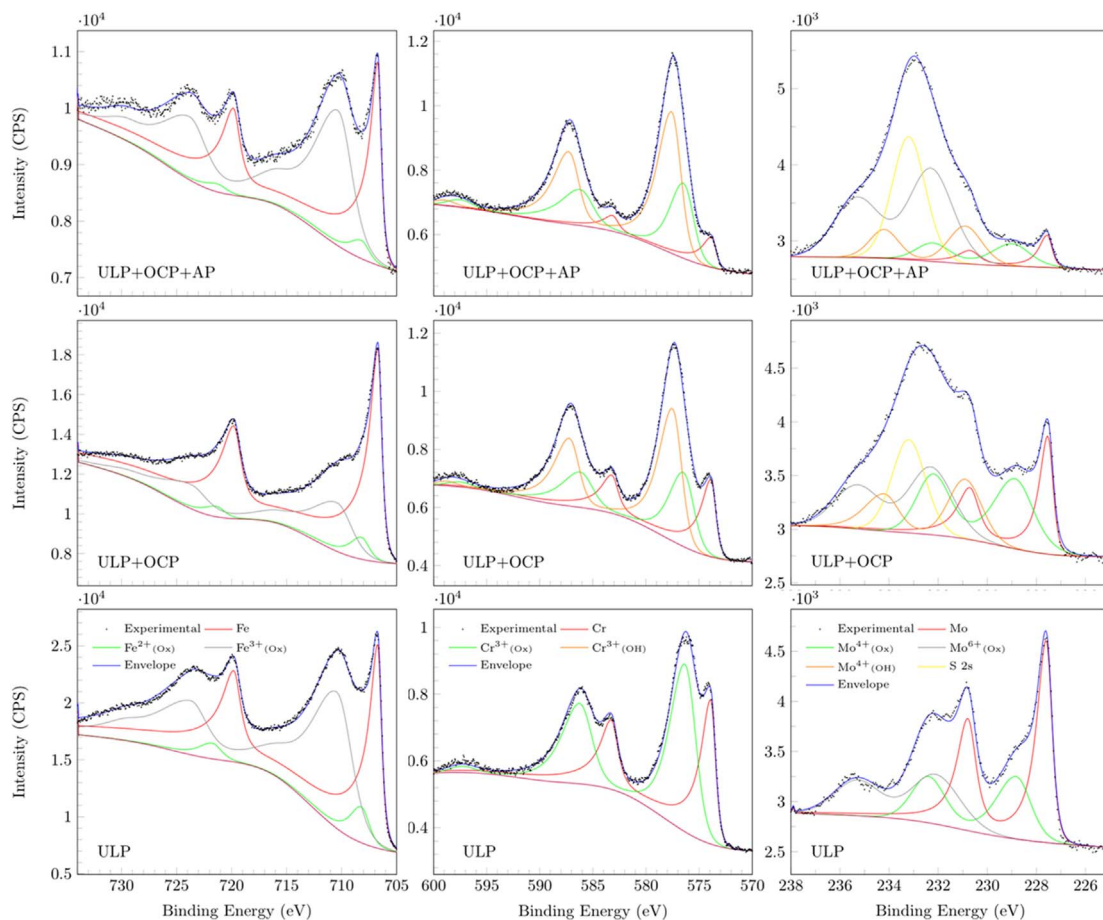


Figure 3. XPS Fe 2p, Cr 2p, Mo 3d core level spectra and their peak fitting for the ULP pre-oxidized 316L surface sequentially treated at open circuit potential (OCP) and under anodic polarization (AP) at $U_{\text{pass}} = 0.025$ V/Pt in 0.05 M H_2SO_4 . The emission angle is 45° .

also needed for curve fitting the Mo 3d region measured after electrochemical treatment. It is assigned to sulfate counter ions originating from the solution. The S $2p_{3/2-1/2}$ doublet, measured at 169.1–170.3 eV after electrochemical treatment, confirms the presence of SO_4^{2-} species adsorbed at the surface of the passive film.

The O 1s spectra obtained before and after electrochemical treatment are shown in Fig. 4. The line shapes show the presence of oxide (O^{2-}), hydroxide (OH^-), sulfate (SO_4^{2-}), and water/oxygen (H_2O) components^{14–16,28,39–41,50,57} with their relative variations for different surface treatments. For the as-prepared initial surfaces, the dominant species are the oxide ligands (O^{2-}) with a stronger hydroxide (OH^-) contribution for the native oxide-covered surface due to contact with water-containing environments after polishing. After electrochemical treatment in $\text{H}_2\text{SO}_4(\text{aq})$, the hydroxide (OH^-) and sulfate (SO_4^{2-}) contributions increase due to hydroxylation of the surface oxide and to the presence of sulfates counter ions adsorbed from the solution. Water ligands would only be present for the electrochemically treated surfaces.

Layered oxide film models.—The equivalent thickness of the oxide layers, as well as the relative atomic concentrations of the different Fe, Cr, Ni and Mo species, were calculated from the XPS data using two different layered oxide film models (Fig. 5). In these models, the different layers are considered uniform in thickness, separated by sharp interfaces, with the oxide or metal components homogeneously distributed in each layer, and the metal signal totally derived from the modified alloy region underneath the oxide. For both models, the intensities of the Fe^0 , Cr^0 , Ni^0 and Mo^0 metal components were assigned to this modified alloy region. The very low intensity of the Ni^{2+} component was neglected.

The single-layer model (Fig. 5a) assumes that all oxide and hydroxide components originate from a single surface oxide layer. Accordingly, the intensities of all $\text{Fe}^{2+/3+}$, Cr^{3+} , and $\text{Mo}^{4+/6+}$ oxide and hydroxide peak components were assigned to the oxide layer. The bilayer model (Fig. 5b) assumes an outer layer that exchanges with the electrolyte and an inner layer being the barrier slowing down atomic transport. Based on hydroxide/oxide bilayer structures previously described,^{4–6,14–16,43,58} all hydroxide and oxide components should be assigned to the outer exchange and inner barrier layers, respectively. However, Time-of-Fight Secondary Ion Mass Spectrometry (ToF-SIMS) depth profiling performed before and after electrochemical passivation of the native oxide-covered polycrystalline AISI 316L surface revealed a marked stratification with oxidized iron and molybdenum preferentially distributed in the exchange outer layer and oxidized chromium in the inner barrier layer.^{39–41} Accordingly, we assigned the intensities of all $\text{Fe}^{2+/3+}$ and $\text{Mo}^{4+/6+}$ oxide and hydroxide peaks to the exchange outer layer and the intensity of the Cr^{3+} oxide component to the barrier inner layer. The Cr^{3+} hydroxide component, only observed after electrochemical treatment, was assigned to the exchange outer layer. This is the same bilayer model as that adopted in our previous work on FeCrNi surfaces,⁴⁰ but with Mo added in the outer layer. The results are shown in Table III and graphically in Fig. 6 for the bilayer model.

Passivation-induced alterations.—*Native oxide-covered surface.*—For the native oxide-covered surface (Table III, Fig. 6), the total thickness is found to be 2.3 nm, with outer and inner layers 1.3 and 1.0 nm thick, respectively. The total value is in good agreement with that (2–2.2 nm) found for the same as-prepared surface of

Table I. Parameters used for fitting the XPS spectra for the native oxide-covered and ULP pre-oxidized 316L stainless steel surfaces before and after electrochemical treatment.

Core level	State	Assignment	BE (± 0.1 eV)	FWHM (± 0.1 eV)
Fe 2p3/2	Fe ⁰	Metal	706.8	0.8
	Fe ²⁺	Oxide	708.3	1.6
	Fe ³⁺	Oxide	710.4	3.1
	Fe ³⁺	Hydroxide	711.5	3.0
	Fe ²⁺	Oxide satellite	712.8	3.7
	Fe ³⁺	Oxide satellite	716.3	4.2
Fe 2p1/2	Fe ⁰	Metal	719.8	1.5
	Fe ²⁺	Oxide	721.8	1.9
	Fe ³⁺	Oxide	723.7	3.6
	Fe ³⁺	Hydroxide	724.5	3.0
	Fe ²⁺	Oxide satellite	726.1	4.1
	Fe ³⁺	Oxide satellite	729.8	4.0
Cr 2p3/2	Cr ⁰	Metal	573.9	1.1
	Cr ³⁺	Oxide	576.4	2.3
	Cr ³⁺	Hydroxide	577.4	2.0
	Cr ³⁺	Oxide satellite	588.5	3.5
	Cr ³⁺	Hydroxide satellite	589.6	3.5
	Cr 2p1/2	Cr ⁰	Metal	583.2
	Cr ³⁺	Oxide	586.1	2.7
	Cr ³⁺	Hydroxide	587.1	2.2
	Cr ³⁺	Oxide satellite	597.4	3.5
	Cr ³⁺	Hydroxide satellite	598.9	3.5
Mo 3d5/2	Mo ⁰	Metal	227.6	0.6
	Mo ⁴⁺	Oxide	229.0	1.7
	Mo ⁴⁺	Hydroxide	230.8	1.5
	Mo ⁶⁺	Oxide	232.2	2.2
Mo 3d3/2	Mo ⁰	Metal	230.8	0.8
	Mo ⁴⁺	Oxide	232.4	1.7
	Mo ⁴⁺	Hydroxide	234.1	1.5
	Mo ⁶⁺	Oxide	235.4	2.2
S 2s	SO ₄ ²⁻	Sulphate	233.1	1.5
Ni 2p3/2	Ni ⁰	Metal	852.8	0.9
	Ni ²⁺	Oxide	855.3	1.5
	Ni ⁰	Metal satellite	858.6	4.4

polycrystalline 316L samples.^{39–41} The overall composition of the film, given by the single-layer model, shows that chromium is already enriched in the oxide film, with Cr³⁺ ions representing 32% of the metal cations. All Cr³⁺ species are found in the barrier inner layer, as assigned by the bilayer model. Consistently, metallic Cr⁰ is found depleted (8 at% instead of 20 at% in the bulk alloy) in the modified alloy underneath the oxide film. Nickel is enriched in the alloy underneath the oxide film (28 at% instead of 12 at% in the bulk alloy), confirming previous studies on this alloy^{39,40} and other austenitic SS.^{9–16} Molybdenum is found enriched in the oxide film (3 at% globally and 5 at% in the exchange outer layer vs 1.6 at% in the bulk alloy). The Mo⁶⁺/Mo⁴⁺ intensity ratio (3.7) shows the marked predominance of Mo⁶⁺ species (Table II). Metallic Mo⁰ concentration is not found significantly altered in the alloy underneath the oxide film (2 at%). The O 1s line shape shows the presence of O²⁻ and OH⁻ ligands with O²⁻ predominance (Fig. 4). The present data show lower Cr³⁺ (32 vs 41%–55% of the metal cations) and Mo^{4+/6+} (3 vs 4%–6%) enrichments than previously measured on the same as-prepared surface of polycrystalline 316L samples.^{39,40} This might be due to differences in rinsing, drying and/or storage conditions. Some studies have reported a decreasing Cr/Fe balance in the native oxide with aging in air.^{15,50,57} Compared to our previous studies,^{39,40} the sample was aged in the glove box before measurement in the present work.

After exposure at OCP in H₂SO₄(aq), the total thickness (1.1 nm) decreases and Cr³⁺ (66 at%) and Mo^{4+/6+} (8 at%) enrichments markedly increase in the oxide film (Table III), confirming the selective iron oxide dissolution previously observed in acid solution in the absence of any applied polarization after direct transfer on this alloy⁴⁰ and austenitic FeCrNi surfaces.⁴⁶ Using the bilayer model, one can infer that iron hydroxide species are dissolved from the exchange outer layer and that chromium oxide species from the inner layer are converted to hydroxide species that concentrate in the exchanged outer layer (Table III, Fig. 6). This explains the decreases in the equivalent thickness of the inner and outer layers. Combined with the stability of the Mo^{4+/6+} species, this mechanism also favors the accumulation of Mo^{4+/6+} species (11 vs 5 at% prior to OCP treatment) in the exchange outer layer. The Mo⁶⁺/Mo⁴⁺ intensity ratio decreases (1.0 vs 3.7 prior to OCP treatment). The O 1s line shape supports marked hydroxylation (Fig. 4), in agreement with the relative decreases of the outer and inner layers in equivalent thickness, also confirming previous measurements performed in the same direct transfer conditions.^{40,46} In the modified alloy underneath the oxide film, the increase of the Fe⁰ and Cr⁰ concentrations balance the decrease of the Ni⁰ concentration. If occurring at OCP, oxide growth is too slow to balance the loss of oxide due to dissolution and does not preferentially consume Fe, Cr and Mo.

Table II. Relative intensities (%) of elemental components of Fe, Cr Mo and Ni for the native oxide-covered and ULP pre-oxidized 316L SS surfaces sequentially treated at open circuit potential (OCP) and under anodic polarization (AP) in 0.05 M H₂SO₄.

Conditions	Fe ⁰ (met)	Fe ²⁺ (ox)	Fe ³⁺ (ox)	Fe ³⁺ (hyd)	Cr ⁰ (met)	Cr ³⁺ (ox)	Cr ³⁺ (hyd)	Mo ⁰ (met)	Mo ⁴⁺ (ox)	Mo ⁴⁺ (hyd)	Mo ⁶⁺ (ox)	Ni ⁰ (met)	Ni ²⁺ (ox)
Nat. Oxide	25	0	54	21	10	90	0	30	15	0	55	82	18
Nat. Oxide + OCP	78	6	17	0	25	26	50	29	16	20	36	100	0
Nat. Oxide + OCP + AP	55	7	39	0	13	43	44	20	14	20	47	93	7
ULP oxide	53	5	42	0	42	58	0	47	26	0	27	100	0
ULP oxide + OCP	74	6	20	0	25	28	47	21	27	31	22	100	0
ULP oxide + OCP + AP	51	3	46	0	10	33	57	8	12	31	49	94	6

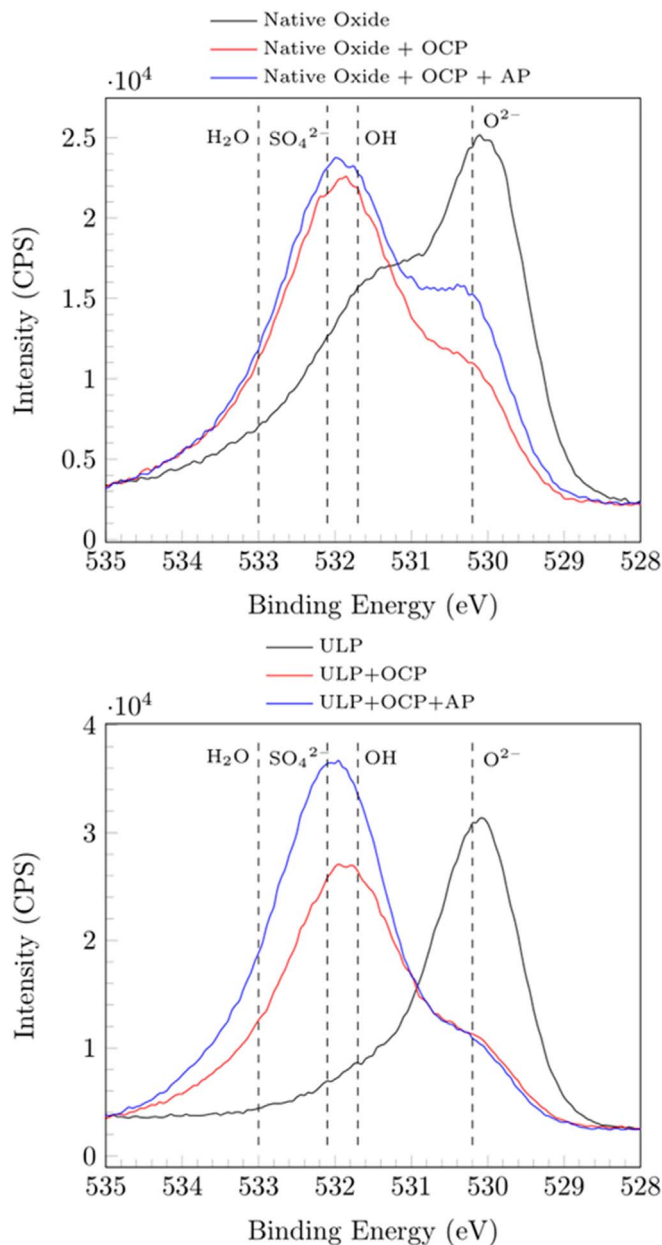


Figure 4. XPS O 1s core level spectra for the native oxide-covered (Nat) and ULP pre-oxidized 316L surfaces sequentially treated at open circuit potential (OCP) and under anodic polarization (AP) in 0.05 M H_2SO_4 . The emission angle is 45° .

After passivation at U_{Pass} in $\text{H}_2\text{SO}_4(\text{aq})$, the total thickness (1.7 nm) of the oxide film increases with the thickening of the outer and inner layers, as shown by the single and bilayer models (Table III, Fig. 6). The increase of the steady-state thickness of the passive film is due to the applied anodic polarization that forces a faster formation of oxide species less rapidly balanced by oxide dissolution. The overall composition of the oxide film shows a slight decrease in Cr^{3+} species but no significant loss of $\text{Mo}^{4+/6+}$ enrichment. The formation of a thicker Cr^{3+} oxide barrier inner layer indicates that the overall loss in chromium enrichment results from a less rapid, because balanced by forced oxide growth, but more competitive iron and chromium oxides dissolution than at OCP. In the exchange outer layer, Mo remains enriched (10 vs 11 at % after treatment at OCP). The $\text{Mo}^{6+}/\text{Mo}^{4+}$ intensity ratio (1.4) increases but not to its initial value (3.7) prior to electrochemical treatment. The O 1s line shape (Fig. 4) shows a decreasing OH/O^{2-}

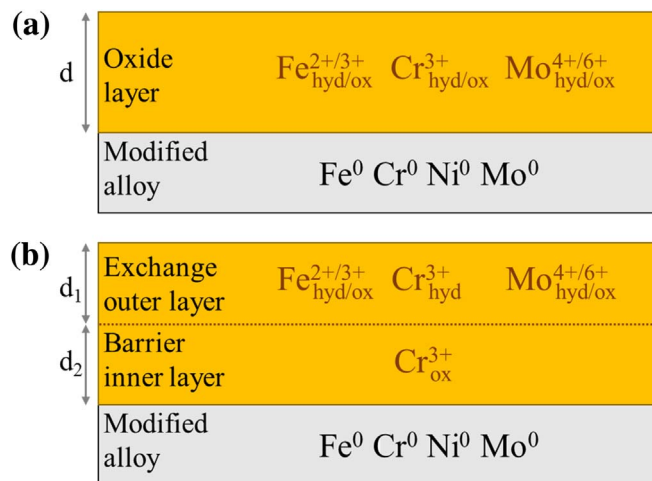


Figure 5. Single-layer (a) and bilayer (b) models of surface oxide film formed on FeCrNiMo stainless steel. Alloy composition underneath the oxide film is modified compared to bulk composition.

balance owing to dehydroxylation under anodic polarization.^{15,16,39–41,44,51,57} Compared to OCP, the Ni enrichment in the modified alloy region increases due to the selective oxidation of Fe and Cr forced by anodic polarization. The Mo^0 concentration is not altered.

ULP pre-oxidized surface.—For the as-prepared ULP pre-oxidized surface, the total thickness is found to be 1.2–1.3 nm depending, on the model, with outer and inner layers 1.0 and 0.3 nm thick, respectively (Table I, Fig. 6). This is markedly lower than for the native oxide-covered surface, confirming the effect of ULP pre-oxidation observed on austenitic FeCrNi surfaces.⁴⁶ The formation of a thinner surface oxide film results from the markedly reduced exposure to water. This is in agreement with the acceleration effect of water observed on the oxidation behavior of SS at high temperatures, but also at RT.⁵⁸ The overall composition of the film obtained with the single-layer model shows a lower chromium enrichment, but suggests increased molybdenum enrichment compared to the native-oxide covered surface. Accordingly, the bilayer model shows a thinner Cr^{3+} inner layer but similar (6 vs 5 at%) $\text{Mo}^{4+/6+}$ enrichment in the outer layer. The $\text{Mo}^{6+}/\text{Mo}^{4+}$ intensity ratio (1.0) is lower than for the native oxide surface. An inner layer equivalent thickness of 0.3 nm suggests the formation of a dispersed barrier layer not fully covering the surface. The modified alloy region is found to be less depleted in chromium and without the enrichment of nickel, compared to the native oxide-covered surface, which is consistent with the formation of a thinner chromium enriched oxide film. Metallic Mo^0 concentration is not found significantly altered in the alloy underneath the ULP oxide film, as seen underneath the native oxide film.

After treatment at OCP, the oxide film does not decrease in thickness like observed for the native oxide-covered surface. However, here again, the increase of the Cr^{3+} and $\text{Mo}^{4+/6+}$ enrichments confirm the preferential dissolution of iron oxide species. The enrichments in Cr^{3+} (56 vs 23 at% prior to OCP treatment) and $\text{Mo}^{4+/6+}$ (13 vs 5 at% prior to OCP treatment) markedly increase in the exchange outer layer of the bilayer model. The $\text{Mo}^{6+}/\text{Mo}^{4+}$ intensity ratio decreases and is lower (0.4) than that obtained for the OCP-treated native oxide-covered sample. The barrier inner layer does not appear altered, despite the accumulation of Cr^{3+} hydroxide species in the outer layer. The O 1s line shape supports marked hydroxylation (Fig. 4), in agreement with the relative increase of Cr^{3+} and Mo^{4+} hydroxide species in the outer layer. The modified metallic region does not show preferential consumption of chromium, nor molybdenum, despite their increased enrichment in the oxide film.

Table III. Equivalent thickness d (nm) and relative concentration (at%) of oxide films and modified alloy regions as calculated using the single and bilayer models for the native oxide-covered and ULP pre-oxidized 316L SS surfaces sequentially treated at open circuit potential (OCP) and under anodic polarization (AP) in 0.05 M H_2SO_4 .

Conditions	Single-layer model				Bilayer model						Modified alloy			
	d	Fe (\pm 2%)	Cr (\pm 2%)	Mo (\pm 2%)	Outer layer			Inner layer			Fe (\pm 2%)	Cr (\pm 2%)	Ni (\pm 2%)	Mo (\pm 2%)
					d_1	Fe (\pm 2%)	Cr (\pm 2%)	Mo (\pm 2%)	d_2	Cr				
Nat. Oxide	2.3 (\pm 0.2)	64	32	3	1.3 (\pm 0.1)	95	0	5	1 (\pm 0.1)	100	62	8	28	2
Nat. Oxide + OCP	1.1 (\pm 0.2)	25	66	8	0.9 (\pm 0.1)	32	56	11	0.3 (\pm 0.1)	100	67	13	17	2
Nat. Oxide + OCP + AP	1.7 (\pm 0.2)	34	59	7	1.2 (\pm 0.1)	47	42	10	0.6 (\pm 0.1)	100	65	12	22	2
ULP oxide	1.2 (\pm 0.1)	73	23	5	1 (\pm 0.1)	94	0	6	0.3 (\pm 0.1)	100	74	13	10	2
ULP oxide + OCP	1.2 (\pm 0.1)	30	56	13	1 (\pm 0.1)	38	44	17	0.3 (\pm 0.1)	100	71	13	13	2
ULP oxide + OCP + AP	2.1 (\pm 0.2)	28	57	15	1.6 (\pm 0.1)	35	46	19	0.6 (\pm 0.1)	100	65	12	21	2

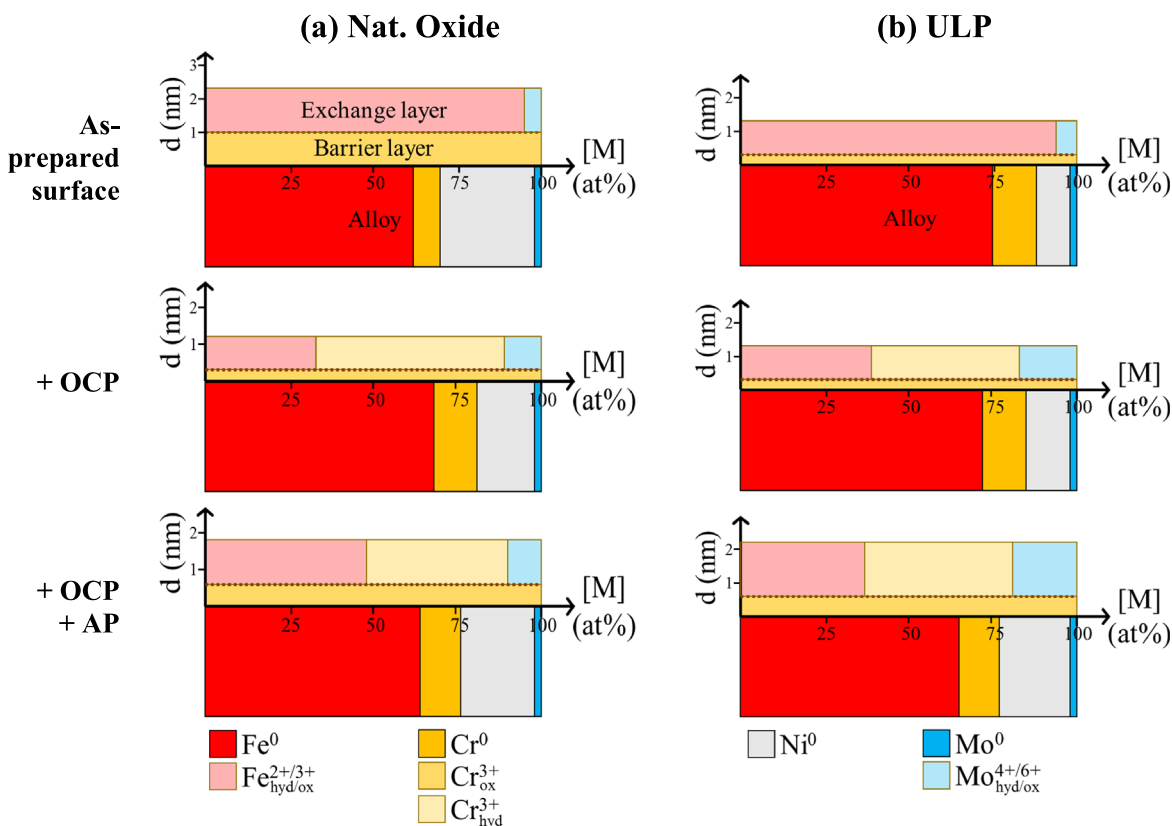


Figure 6. Graph representation of equivalent thickness and relative concentration of the oxide films and modified alloy regions as calculated using the bilayer model for the native oxide-covered (a) and ULP pre-oxidized (b) 316L SS surfaces sequentially treated at open circuit potential (OCP) and under anodic polarization (AP) in 0.05 M H_2SO_4 .

After anodic polarization at U_{Pass} , the total thickness of the oxide film increases with the thickening of the exchange outer and barrier inner layers (Table III, Fig. 6). The increase of the steady-state thickness of the passive film upon applied anodic polarization is confirmed. Enrichment in Cr^{3+} and $\text{Mo}^{4+/6+}$ species in the exchange outer layer does not significantly increase, but these species are accumulated owing to the increase in thickness. The $\text{Mo}^{6+}/\text{Mo}^{4+}$ intensity ratio increases (1.1). Cr^{3+} species also accumulate in the inner layer to form a thicker barrier, like for the native oxide-covered surface. The O 1s line shape suggests that hydroxylation remains high (Fig. 4). The composition of the modified alloy region shows preferential consumption of iron. Mo^0 concentration remains unaltered.

Effects of pre-oxidation.—Comparison of the native oxide-covered and ULP pre-treated surfaces after OCP treatment allows us to discuss the differences in passivation behavior revealed by the polarization curves (Fig. 1). Indeed, the curves were measured after OCP in the same conditions as for XPS analysis. After OCP exposure, the surface oxide films have similar total thickness, including the exchange outer and barrier inner layers. For the ULP pre-oxidized surface, Cr^{3+} enrichment is globally lower due to lower concentration in the exchange outer layer, however, $\text{Mo}^{4+/6+}$ enrichment in the exchange outer layer is higher. The $\text{Mo}^{6+}/\text{Mo}^{4+}$ ratio is lower. The barrier inner layer, assumed to be 100 at% Cr^{3+} , has the same thickness. In the modified alloy region, metallic Ni^0 is less enriched, and Cr^0 similarly depleted. Metallic Mo^0 concentration is the same.

Two effects may combine to promote the passivation efficiency observed for the ULP pre-oxidized surface. Transient active dissolution can be retarded by the marked enrichment in Mo^0 of the modified metallic alloy underneath the surface oxide film, thus contributing to suppress the activation peak. This effect of Mo^0

enrichment on active dissolution has been previously proposed to explain improved resistance to the initiation of pitting by enhanced re-passivation after passivity breakdown.^{11,13,18,29,31–34} It was observed for surfaces passivated in Cl-containing solution. In the present work, performed with direct transfer to surface analysis, we observed no significant Mo^0 enrichment (nor depletion) in the modified alloy region and no effect of ULP pre-oxidation for surfaces exposed to Cl-free solution in OCP conditions. The other effect promoting passivation efficiency can relate to the protection properties of the surface oxide. $\text{Mo}^{4+/6+}$ enrichment could promote the sealing properties of the exchange outer layer. Thus, even though the barrier inner layer is equally thick and rich in Cr^{3+} oxide on the ULP pre-oxidized surface, its chemical/morphological imperfections could be better healed by an outer layer more abundant in $\text{Mo}^{4+/6+}$ species. This effect is in agreement with the previously proposed retarding effect of molybdenum on the entry of depassivating species (i.e. chlorides).^{9,17,19–21,27,28} A comparison of the as-prepared surfaces shows that the difference in $\text{Mo}^{4+/6+}$ enrichment is not obtained after the initial pre-oxidation treatment but after treatment at OCP.

After anodic polarization at U_{Pass} of the ULP pre-oxidized surface, Mo^0 concentration in the modified alloy region remains unaltered and $\text{Mo}^{4+/6+}$ accumulation in the exchange outer layer increases owing to thickening. Global $\text{Mo}^{4+/6+}$ enrichment is thus markedly higher than observed on the native oxide-covered surface, like proposed from in situ photoelectrochemical measurements.²⁵ Thus, one can expect the ULP pre-oxidation treatment to also provide improved sealing properties to the exchange outer layer formed after anodic polarization, thereby retarding the entry of aggressive species promoting depassivation. Note that re-passivation properties after passivity breakdown would not be affected since Mo^0 concentration in the modified alloy region is not altered by the ULP pre-treatment.

Conclusions

A closed system, with direct transfer line avoiding exposure to ambient air, between UHV analytical platform for surface preparation and analysis and Ar-filled glove box equipped for electrochemical treatment was used to study the effects of controlled pre-oxidation at low oxygen pressure on the passivation mechanisms of polycrystalline 316L SS surfaces. XPS was applied before and after electrochemical treatment at OCP and anodic passivation and the measured composition and thickness of the surface oxide films were quantitatively discussed using layered oxide film models.

On the native oxide-covered surface obtained after polishing, the passivation mechanism is characterized by marked preferential dissolution of oxidized iron already occurring at OCP. The steady-state thickness of the initially formed oxide film decreases, however, its enrichment in Cr³⁺ and Mo^{4+/6+} is promoted, mostly in the exchange outer hydroxide layer. Anodic polarization in the passive range causes the steady-state thickness to increase owing to oxide growth less rapidly balanced by oxide dissolution. The barrier inner oxide layer of the passive film becomes thicker while the exchange outer layer is less Cr³⁺-rich, but maintains the Mo^{4+/6+} enrichment obtained at OCP. Metallic Mo concentration is unaltered in the modified alloy region underneath the oxide film compared to the initial surface state.

On the pre-oxidized surface, prepared at low oxygen pressure and room temperature, the oxide film grown at saturation is thinner than on the native oxide-covered surface due to minimization of the promoting effect of water on the surface oxidation kinetics. The formation of the inner layer is limited to less than an equivalent monolayer (i.e., not continuous) and the outer layer thinner but equally enriched in Mo^{4+/6+} than on the native oxide-covered surface. Mo concentration is unaltered in the modified alloy region underneath the oxide film. At OCP, preferential dissolution of oxidized iron also promotes the Cr³⁺ and Mo^{4+/6+} enrichment. However, molybdenum enrichment is markedly increased in the exchange outer layer compared to the native oxide-covered surface, which improves the protectiveness against transient active dissolution during the active/passive transition. Anodic passivation increases the steady-state thickness like on the native oxide-covered surface but with higher Mo-enrichment in the exchange outer layer.

This work brings new insight on the long-debated effects of molybdenum on the passivity of stainless steel. It shows that, by promoting the surface molybdenum enrichment, controlled pre-oxidation can be expected to benefit the sealing properties of the exchange outer layer of the passive film against the ingress of aggressive ions (i.e., chlorides) without altering the repassivation properties of the modified alloy region after passivity breakdown.

Acknowledgments

This project has received funding from the European Research Council (ERC) under the European Union's Horizon 2020 research and innovation program (ERC Advanced grant no. 741123, Corrosion Initiation Mechanisms at the Nanometric and Atomic Scales: CIMNAS). Région Île-de-France is acknowledged for partial funding of the XPS and STM equipment. China Scholarship Council (CSC) is acknowledged for the scholarship to Li Ma (no. 201606380129).

ORCID

Benjamin Lynch  <https://orcid.org/0000-0002-1379-495X>
 Zuocheng Wang  <https://orcid.org/0000-0001-8846-005X>
 Li Ma  <https://orcid.org/0000-0003-4677-5533>
 Frédéric Wiame  <https://orcid.org/0000-0002-1422-6858>
 Vincent Maurice  <https://orcid.org/0000-0001-5222-997>
 Philippe Marcus  <https://orcid.org/0000-0002-9140-0047>

References

1. D. Macdonald, "Passivity - the key to our metals-based civilization." *Pure Appl. Chem.*, **71**, 951 (1999).
2. P. Schmuki, "From Bacon to barriers: a review on the passivity of metals and alloys." *J. Solid State Electrochem.*, **6**, 145 (2002).
3. C. Olsson and D. Landolt, "Passive films on stainless steels - chemistry, structure and growth." *Electrochimica Acta*, **48**, 1093 (2003).
4. H.-H. Strehblow, V. Maurice, and P. Marcus, "Passivity of metals." *Corrosion Mechanisms in Theory and Practice*, ed. P. Marcus (Taylor and Francis, CRC Press, United States of America) 3rd ed., p. 235 (2011).
5. P. Marcus and V. Maurice, "Oxide passive films and corrosion protection." *Sci. Technol.*, ed. G. Pacchioni and S. Valeri (Wiley-VCH Verlag GmbH & Co. KGaA, Weinheim) p. 119 (2012).
6. H.-H. Strehblow, "Passivity of metals studied by surface analytical methods, a review." *Electrochim. Acta*, **212**, 630 (2016).
7. V. Maurice and P. Marcus, "Progress in corrosion science at atomic and nanometric scales." *Prog. Mater. Sci.*, **95**, 132 (2018).
8. V. Maurice and P. Marcus, "Current developments of nanoscale insight into corrosion protection by passive oxide films." *Curr. Opin. Solid State Mater. Sci.*, **22**, 156 (2018).
9. K. Sugimoto and Y. Sawada, "The role of molybdenum additions to austenitic stainless steels in the inhibition of pitting in acid chloride solutions." *Corros. Sci.*, **17**, 425 (1977).
10. H. Ogawa, H. Omata, I. Itoh, and H. Okada, "Auger electron spectroscopic and electrochemical analysis of the effect of alloying elements on the passivation behavior of stainless steels." *Corrosion*, **34**, 52 (1978).
11. I. Olefjord, "The passive state of stainless steels." *Materials Science and Engineering*, **42**, 161 (1980).
12. I. Olefjord and B.-O. Elfstrom, "The composition of the surface during passivation of stainless steels." *Corrosion*, **38**, 46 (1982).
13. A. R. Brooks, C. R. Clayton, K. Doss, and Y. C. Lu, "On the role of cr in the passivity of stainless steel." *J. Electrochem. Soc.*, **133**, 2459 (1986).
14. E. De Vito and P. Marcus, "XPS study of passive films formed on molybdenum-implanted austenitic stainless steels." *Surf. Interface Anal.*, **19**, 403 (1992).
15. V. Maurice, W. P. Yang, and P. Marcus, "X-Ray photoelectron spectroscopy and scanning tunneling microscopy study of passive films formed on (100) Fe-18Cr-13Ni single-crystal surfaces." *J. Electrochem. Soc.*, **145**, 909 (1998).
16. V. Maurice, H. Peng, L. H. Klein, A. Seyeux, S. Zanna, and P. Marcus, "Effects of molybdenum on the composition and nanoscale morphology of passivated austenitic stainless steel surfaces." *Faraday Discuss.*, **180**, 151 (2015).
17. J. E. Castle and J. H. Qiu, "A co-ordinated study of the passivation of alloy steels by plasma source mass spectrometry and X-ray photoelectron spectroscopy—I. characterization of the passive film." *Corros. Sci.*, **29**, 591 (1989).
18. I. Olefjord, B. Brox, and U. Jelvestam, "Surface composition of stainless steels during anodic dissolution and passivation studied by ESCA." *J. Electrochem. Soc.*, **132**, 2854 (1985).
19. C. R. Clayton and Y. C. Lu, "A bipolar model of the passivity of stainless steel: the role of mo addition." *J. Electrochem. Soc.*, **133**, 2465 (1985).
20. Y. C. Lu, C. R. Clayton, and A. R. Brooks, "A bipolar model of the passivity of stainless steels—II." *The Influence of Aqueous Molybdate, Corrosion Science*, **29**, 863 (1989).
21. C. R. Clayton and Y. C. Lu, "A bipolar model of the passivity of stainless steels—III. The mechanism of MoO₄²⁻ formation and incorporation." *Corros. Sci.*, **29**, 881 (1989).
22. I. Olefjord and L. Wegrelius, "Surface analysis of passive state." *Corros. Sci.*, **31**, 89 (1990).
23. M. Santamaria, F. Di Franco, F. Di Quarto, M. Pisarek, S. Zanna, and P. Marcus, *J. Solid State Electrochem.*, **19**, 3511 (2015).
24. D.-H. Xia, Y. Behnamian, and J.-L. Luo, *J. Electrochem. Soc.*, **166**, C49 (2019).
25. G. Tranchida, F. Di Franco, and M. Santamaria, *J. Electrochem. Soc.*, **167**, 061506.
26. M.-W. Tan, E. Akiyama, A. Kawashima, K. Asami, and K. Hashimoto, "The effect of air exposure on the corrosion behavior of amorphous Fe-8Cr-Mo-13P-7C alloys in 1 M HCl." *Corros. Sci.*, **37**, 1289 (1995).
27. D. D. Macdonald, "The point defect model for the passive state." *J. Electrochem. Soc.*, **139**, 3434 (1992).
28. A. Elbiache and P. Marcus, "The role of molybdenum in the dissolution and the passivation of stainless steels with adsorbed sulphur." *Corros. Sci.*, **33**, 261 (1992).
29. R. f. a Jargelius-Pettersson, "Electrochemical investigation of the influence of nitrogen alloying on pitting corrosion of austenitic stainless steels." *Corros. Sci.*, **41**, 1639 (1999).
30. L. Wegrelius, F. Falkenberg, and I. Olefjord, "Passivation of stainless steels in hydrochloric acid." *J. Electrochem. Soc.*, **146**, 1397 (1999).
31. G. O. Ilevbare and G. T. Burstein, "The role of alloyed molybdenum in the inhibition of pitting corrosion in stainless steels." *Corros. Sci.*, **43**, 485 (2001).
32. A. Pardo, M. C. Merino, A. E. Coy, F. Viejo, R. Arrabal, and E. Matykina, "Effect of Mo and Mn additions on the corrosion behaviour of AISI 304 and 316 stainless steels in H₂SO₄." *Corros. Sci.*, **50**, 780 (2008).
33. A. Pardo, M. C. Merino, A. E. Coy, F. Viejo, R. Arrabal, and E. Matykina, "Pitting corrosion behaviour of austenitic stainless steels – combining effects of Mn and Mo additions." *Corros. Sci.*, **50**, 1796 (2008).
34. K. Hashimoto, K. Asami, and K. Teramoto, "An X-ray photo-electron spectroscopic study on the role of molybdenum in increasing the corrosion resistance of ferritic stainless steels in HCl." *Corros. Sci.*, **19**, 3 (1979).

35. L. Ma, F. Wiame, V. Maurice, and P. Marcus, "New insight on early oxidation stages of austenitic stainless steel from in situ XPS analysis on single-crystalline Fe-18Cr-13Ni(100)." *Corros. Sci.*, **140**, 205 (2018).
36. L. Ma, F. Wiame, V. Maurice, and P. Marcus, "Origin of nanoscale heterogeneity in the surface oxide film protecting stainless steel against corrosion." *Npj Materials Degradation*, **3**, 1 (2019).
37. L. Ma, F. Wiame, V. Maurice, and P. Marcus, "Stainless steel surface structure and initial oxidation at nanometric and atomic scales." *Appl. Surf. Sci.*, **494**, 8 (2019).
38. T. Massoud, V. Maurice, L. H. Klein, A. Seyeux, and P. Marcus, "Nanostructure and local properties of oxide layers grown on stainless steel in simulated pressurized water reactor environment." *Corros. Sci.*, **84**, 198 (2014).
39. Z. Wang, F. Di-Franco, A. Seyeux, S. Zanna, V. Maurice, and P. Marcus, "Passivation-induced physicochemical alterations of the native surface oxide film on 316L austenitic stainless steel." *J. Electrochem. Soc.*, **166**, C3376 (2019).
40. Z. Wang, E.-M. Paschalidou, A. Seyeux, S. Zanna, V. Maurice, and P. Marcus, "Mechanisms of Cr and Mo enrichments in the passive oxide film on 316L austenitic stainless steel, *Frontiers in.*" *Materials*, **6**, 232 (2019).
41. Z. Wang, A. Seyeux, S. Zanna, V. Maurice, and P. Marcus, "Chloride-induced alterations of the passive film on 316L stainless steel and blocking effect of pre-passivation." *Electrochim. Acta*, **329**, 135 (2020).
42. C. Leygraf, G. Hultquist, I. Olefjord, B.-O. Elfström, V. M. Knyazheva, A. V. Plaskheyev, and Y. M. Kolotyrlin, "Selective dissolution and surface enrichment of alloy components of passivated Fe18Cr and Fe18Cr3Mo single crystals." *Corros. Sci.*, **19**, 343 (1979).
43. G. Hultquist, M. Seo, T. Leitner, C. Leygraf, and N. Sato, "The dissolution behaviour of iron, chromium, molybdenum and copper from pure metals and from ferritic stainless steels." *Corros. Sci.*, **27**, 937 (1987).
44. P. Keller and H.-H. Strehblow, "XPS investigations of electrochemically formed passive layers on Fe/Cr-alloys in 0.5 M H₂SO₄." *Corros. Sci.*, **46**, 1939 (2004).
45. G. Tranchida, M. Clesi, F. Di Franco, F. Di Quarto, and M. Santamaria, *Electrochim. Acta*, **273**, 412 (2018).
46. L. Ma, E.-M. Paschalidou, F. Wiame, S. Zanna, V. Maurice, and P. Marcus, "Passivation mechanisms and pre-oxidation effects on model surfaces of FeCrNi austenitic stainless steel." *Corros. Sci.*, **167**, 108483 (2020).
47. T. Massoud, V. Maurice, L. H. Klein, and P. Marcus, "Nanoscale morphology and atomic structure of passive films on stainless steel." *J. Electrochem. Soc.*, **160**, C232 (2013).
48. www.casaxps.com (2018).
49. A. M. Salvi, J. E. Castle, J. F. Watts, and E. Desimoni, "Peak fitting of the chromium 2p XPS spectrum." *Appl. Surf. Sci.*, **90**, 333 (1995).
50. V. Maurice, W. P. Yang, and P. Marcus, "XPS and STM study of passive films formed on Fe-22Cr(110) single-crystal surfaces." *J. Electrochem. Soc.*, **143**, 1182 (1996).
51. S. Yuan and S. Pehkonen, "Microbiologically influenced corrosion of 304 stainless steel by aerobic Pseudomonas NCIMB 2021 bacteria: AFM and XPS study." *Colloids Surf., B*, **59**, 87 (2007).
52. H. Sun, X. Q. Wu, and E. H. Han, "Effects of temperature on the oxide film properties of 304 stainless steel in high temperature lithium borate buffer solution." *Corros. Sci.*, **51**, 2840 (2009).
53. M. C. Biesinger, B. P. Payne, A. P. Grosvenor, L. W. M. Lau, A. R. Gerson, and R. S. C. Smart, "Resolving surface chemical states in XPS analysis of first row transition metals, oxides and hydroxides: Cr, Mn, Fe, Co and Ni." *Appl. Surf. Sci.*, **257**, 2717 (2011).
54. M. Aronniemi, J. Sainio, and J. Lahtinen, "Chemical state quantification of iron and chromium oxides using XPS: the effect of the background subtraction method." *Surf. Sci.*, **578**, 108 (2005).
55. W. Yang, R.-C. Ni, H.-Z. Hua, and A. Pourbaix, "The behavior of chromium and molybdenum in the propagation process of localized corrosion of steels." *Corros. Sci.*, **24**, 691 (1984).
56. P. Spevack and N. McIntyre, "Thermal reduction of molybdenum trioxide." *J. Phys. Chem.*, **96**, 9029 (1992).
57. W. P. Yang, D. Costa, and P. Marcus, "Resistance to pitting and chemical composition of passive films of a Fe-17%Cr alloy in chloride-containing acid solution." *J. Electrochem. Soc.*, **141**, 2669 (1994).
58. S. R. J. Saunders, M. Monteiro, and F. Rizzo, "The oxidation behaviour of metals and alloys at high temperatures in atmospheres containing water vapour: A review." *Prog. Mater Sci.*, **53**, 775 (2008).